High-performance polarization-sensitive photodetectors based on aligned-CNT/WSe_2 heterojunctions

Wenkai Zhu(朱文凯)[1,2,#], Ke Yan(严可)[3,#],Yong Zhang(张勇)[3], Shuai Huo(霍帅)[3], Zhen Zhang(张真)[3], Zhonghui Li(李忠辉)[3,†], Yang Yang(杨扬)[3,†], Kaiyou Wang(王开友)[1,2,†]

[1]State Key Laboratory of Semiconductor Physics and Chip Technologies, Institute of Semiconductors, Chinese Academy of Sciences, Beijing 100083, China.
[2]College of Materials Science and Opto-Electronic Technology, University of Chinese Academy of Sciences, Beijing 100049, China.
[3]CETC Key Laboratory of Carbon-based Electronics, Nanjing 210016, China
[#]These authors contributed equally to this work.
[†]Corresponding author. E-mail: zhonghuili@126.com, yangyang555@cetc.com.cn, kywang@semi.ac.cn

Abstract

Benefiting from their unique quasi-one-dimensional structure, tunable bandgap, large specific surface area and controllable directional growth features, carbon nanotubes (CNTs) are considered promising candidates for high-performance polarized photodetection. However, most photodetectors reported to date based on CNT films still deliver relatively low polarization anisotropy ratios, which severely restricts their practical deployment. In this work, we fabricate a novel polarization-sensitive photodetector based on a one-dimensional (1D)/two-dimensional (2D) heterostructure composed of highly aligned, horizontally arranged, densely packed-CNTs and WSe_2. The device achieves a high responsivity of 10.6 A/W at 550 nm together with a response time of 2.5 ms. Notably, it displays strong polarization-dependent absorption in the 660-920 nm wavelength range. Under self-powered operating conditions, the maximum linear polarization anisotropy ratio reaches 2.9 at 880 nm. This work lays an experimental foundation for the construction of high-performance polarization photodetectors utilizing 1D/2D aligned-CNT/semiconductor p-n junctions.

Keywords: carbon nanotube, aligned CNT film, photodetection, polarization anisotropy ratio

PACS: 61.48.De, 85.60.Gz, 42.79.Ci

1. Introduction

Polarized photodetectors capable of resolving the polarization state of light possess strong penetration capability and high polarization discrimination, and are widely utilized in polarization imaging, polarized optical communication, target recognition, remote sensing and medical diagnosis.[1-5] Owing to their quasi-one-dimensional (1D) geometry and tunable band structure, carbon nanotubes (CNTs) exhibit distinctive potential for polarized photodetection applications.[6-8] An individual CNT shows strong anisotropic absorption toward linearly polarized light: it efficiently absorbs light polarized parallel to its tube axis while suppressing absorption of transversely polarized light.[9] Nevertheless, photodetectors constructed from individual CNTs suffer from insufficient light absorption capacity. Meanwhile, films consisting of randomly oriented CNTs fail to produce obvious polarization-dependent absorption due to carrier transport between adjacent nanotubes. Large-area highly aligned CNT films have been fabricated via vacuum filtration technique,[10,11] the Langmuir-Blodgett (LB) method,[12] self-assembly approaches,[13-15] and in-situ chemical vapor deposition (CVD) for vertically aligned CNT arrays,[16] which lays a solid foundation for developing CNT-based polarized photodetectors. Despite outstanding optoelectronic characteristics such as high responsivity,[17,18] ultrafast response speed[19-21] and broadband photoresponse,[22-24] photodetectors based on CNT films deliver unsatisfactory polarized photodetection performance that requires substantial optimization.[25]

Metallic-phase CNTs are inevitably incorporated during the growth of semiconducting-CNT films, which gives rise to a high dark current of the devices.[26] Therefore, suppressing the dark current is the primary requirement to improve the signal-to-noise ratio of the photocurrent in CNT-based photodetectors.[27] Several strategies, including constructing p-n junctions through chemical doping or electrostatic gating,[26,28-30] and adopting asymmetric metal electrodes with distinct work functions,[31] have been proved to strengthen the built-in electric field of CNT photodetectors, boost the extraction efficiency of photogenerated carriers, and thereby

enhance responsivity, while effectively suppressing dark current. More interestingly, hybrid structures of aligned CNTs and quasi-1D TiO_2 nanowire arrays were fabricated by taking advantage of the structural anisotropy of 1D aligned CNTs and nanowires. The composite devices exhibited a polarized photocurrent ratio of 1.5 under ultraviolet irradiation.[32] In addition, fabricating 1D/two-dimensional (2D) hybrid systems composed of CNTs and 2D van der Waals semiconductors has been verified as an effective route to simultaneously improve responsivity and polarization anisotropy ratio.[33] For instance, Huang et al. reported mixed-dimensional CNT/MoS_2 heterostructure photodetectors. Such devices operate in self-powered mode covering the visible spectral range of 405-785 nm and exhibit polarization-sensitive photoresponse, yielding a polarization anisotropy ratio of 1.55 under 532 nm laser illumination.[34] However, the responsivity and polarization anisotropy ratio of the 1D/2D hybrid devices are still unsatisfactory, and their polarization-dependent capabilities need to be further optimized.[35,36]

As a typical 2D transition metal dichalcogenide (TMD), multilayer WSe_2 exhibits n-type semiconductor conductivity, high carrier mobility, and strong light-matter interaction, making it promising for high-performance photodetectors.[37] Nevertheless, the highly symmetric hexagonal lattice structure of WSe_2 leads to negligible sensitivity to linearly polarized light, limiting its applications in polarized photodetection. Herein, we construct mixed 1D/2D photodetectors based on macroscopically aligned CNTs and 2D WSe_2 heterostructures. Benefiting from the built-in electric field of the p-n junction, the device effectively suppresses dark current, improves the signal-to-noise ratio, and enables self-powered operation. The fabricated device achieves a high responsivity of 10.6 A/W and a response time of 2.5 ms. Moreover, it exhibits robust polarized light absorption within the spectral range of 660-920 nm. A maximum linear polarization anisotropy ratio of 2.9 is realized at 880 nm under self-powered operation. This work provides reliable experimental support for the design and fabrication of high-performance polarization-sensitive photodetectors based on aligned-CNT/semiconductor p-n junctions.

2. Experimental methods

The single-layer aligned CNT films used in this work are synthesized via solution-based self-assembly method, with tube diameters ranging from 1.2 nm to 1.8 nm. The aligned-CNT array is densely packed at a density of 250 tubes per

micrometer. Compared with an individual carbon nanotube, such densely packed arrays enhance light absorption while retaining the intrinsic polarization-dependent absorption characteristics of CNTs. The detailed fabrication process of the aligned-CNTs/WSe_2 heterojunction photodetector is described as follows. First, patterned aligned CNT regions are obtained via photolithography and oxygen plasma etching. Subsequently, Cr/Au metal electrodes with thicknesses of 10 nm and 50 nm are deposited by photolithography combined with high-vacuum magnetron sputtering. A spacing of 5 μm is reserved between the patterned CNT region and one side of the metal electrode for the subsequent integration of WSe_2. The bulk WSe_2 single crystals used in this work are purchased from HQ Graphene. WSe_2 nanosheets are prepared through mechanical exfoliation and 2D dry-transfer method. In detail, WSe_2 nanosheets are mechanically exfoliated onto a polydimethylsiloxane (PDMS) stamp using adhesive tape, and the PDMS stamp is fixed on a glass slide. Based on the optical contrast under an optical microscope,[38] high-quality WSe_2 nanosheets with a thickness of approximately 50 nm and suitable lateral size are selected. With the assistance of a high-precision position-controllable dry-transfer system for 2D materials, one end of the WSe_2 nanosheet is transferred onto the aligned CNT region, while the other end is connected to the metal electrode, forming a complete aligned-CNTs/WSe_2 heterojunction photodetector device. Similarly, individual aligned-CNT and WSe_2 field-effect transistors (FETs) are fabricated using the same process to characterize the intrinsic optoelectronic properties of each material.

The optoelectronic measurement system consists of a supercontinuum laser (Model FP1060, Fianium Ltd.) covering a spectral range of 390-2400 nm, an Omni-λ300 grating monochromator (Zolix Instruments Co., Ltd.), an optical fiber collimation system, 10× objective lenses (Olympus), and a semiconductor parameter analyzer (Agilent B1500A). The beam collimation system is composed of an input objective lens, optical fiber and an output objective lens. Both the input and output objectives are 10× objective lenses from Olympus. For response time characterization, a function generator (Model DG1032Z, Rigol) for voltage application, an optical chopper (Model SR540), a low-noise current preamplifier (Model SR570), and an oscilloscope (Tektronix TDS2022B) are also incorporated. The polarization-dependent photocurrent measurement setup includes a lock-in amplifier (Model SR860), an optical chopper (Model SR540), a Glan-Taylor polarizer, a half-wave plate, a motorized rotary stage (Model RAK100, Zolix Instruments) for precise angular adjustment, and 100× objective lenses (Olympus). Unless otherwise specified, all

optoelectronic measurements were performed at room temperature.

First-principles calculations based on density functional theory (DFT) were performed using the Vienna Ab initio Simulation Package (VASP). The projector-augmented wave (PAW) method was employed to describe the electron-ion interactions; The exchange-correlation energy was treated using the generalized gradient approximation (GGA) of Perdew-Burke-Ernzerhof (PBE). For the geometry optimization and static self-consistent field (SCF) calculations, a plane-wave cutoff energy of 400 eV was used. The electronic and ionic convergence criteria were set to 10^{-6} eV and 10^{-2} eV/Å, respectively. Gaussian smearing (ISMEAR = 0) with a width of $\sigma = 0.05$ eV was applied. To investigate the optical properties of WSe_2/CNT heterostructure, the frequency-dependent complex dielectric function $\varepsilon(\omega) = \varepsilon_1(\omega) + i\varepsilon_2(\omega)$ was evaluated within the independent-particle approximation by setting LOPTICS = .TRUE. The imaginary part $\varepsilon_2(\omega)$ was determined via summation over unoccupied electronic states, while the real part $\varepsilon_1(\omega)$ was derived using the Kramers-Kronig relation. To ensure sufficient coverage of high-energy virtual states and guarantee the convergence of the optical spectra, the total number of electronic bands (NBANDS) was explicitly increased to 502 alongside a refined k-point mesh. Post-processing of the dielectric matrix data was conducted using the VASPKIT package to extract the frequency-dependent macro-optical constants, including the refractive index, absorption coefficient, and reflectivity.

3. Results and discussion

The electrical properties of pristine aligned CNTs and pure WSe_2 were systematically characterized, and the corresponding test results are displayed in Fig. 1. The output *I-V* curves of the Au/aligned-CNT/Au FET in Fig. 1(a) exhibit weak nonlinear transport behavior. This phenomenon originates from the unavoidable coexistence of metallic and semiconducting CNTs grown, resulting in a hybrid conductive system in the CNT film.[26] The temperature-dependent resistance measurements in Fig. 1(b) show a linear reduction in resistance with increasing temperature, indicating that charge transport in the aligned CNT film is predominantly governed by semiconducting CNTs. Furthermore, the transfer characteristics in Fig. 1(c) and 1(d) confirm that aligned CNTs show p-type hole-dominated conduction, while multilayer WSe_2 exhibits n-type electron conduction.[37] The electronic conduction type is determined by the band structure of WSe_2 and the relative position between the Fermi level of the electrode and WSe_2.[39] Such complementary

conductivity enables the construction of high-performance aligned-CNT/WSe_2 p-n heterojunction photodetector devices.

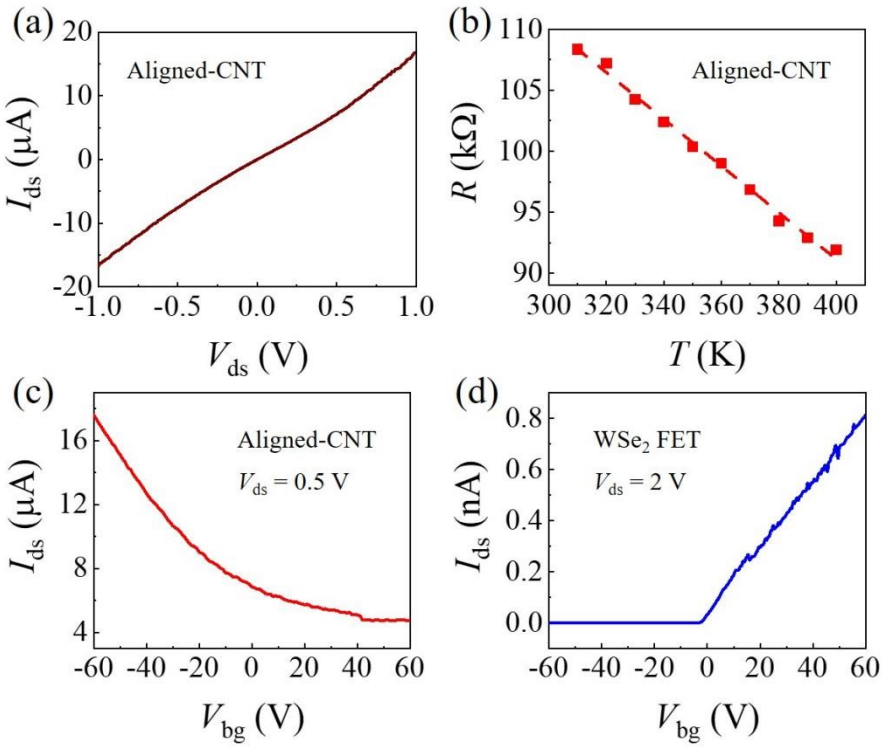


Fig. 1. Electrical characterization of individual aligned CNTs and WSe_2. (a) *I-V* curves of individual aligned CNTs field-effect transistor (FET). (b) Temperature-dependent resistance curves of individual aligned CNTs. The transfer curves for individual aligned CNTs (c) and WSe_2 (d), respectively.

Accordingly, we fabricated p-CNT/n-WSe_2 heterojunction photodetectors. The optical microscope image of the device is displayed in Fig. 2(a). As revealed by scanning electron microscope (SEM) characterization, the axial direction of the CNTs is aligned along the applied current direction (Fig. 2(b)). Such well-ordered arrangement serves as the physical foundation for the device to realize polarized light detection. The as-grown aligned CNT films are monolayers with a tube diameter of approximately 1.5 nm. The semiconducting CNTs owns direct bandgap, which can be calculated using the well-established formula: $E_g \approx \frac{0.88(eV \cdot nm)}{d(nm)}$, where d represents the diameter of single-walled carbon nanotubes.[40,41] The calculated bandgap of the prepared CNT array is about 0.59 eV. The energy band alignment diagram of the

p-CNT/n-WSe_2 heterojunction is presented in Fig. 2(c), which demonstrates a typical type-III band structure. This configuration strengthens the built-in electric field, facilitates the separation of photogenerated charge carriers at the junction, and thus improves the photoresponsivity. Meanwhile, it also suppresses the dark current[42]. In addition, the p-CNT/n-WSe_2 heterojunction device exhibits distinct rectifying characteristics, as shown in Fig. 2(d).

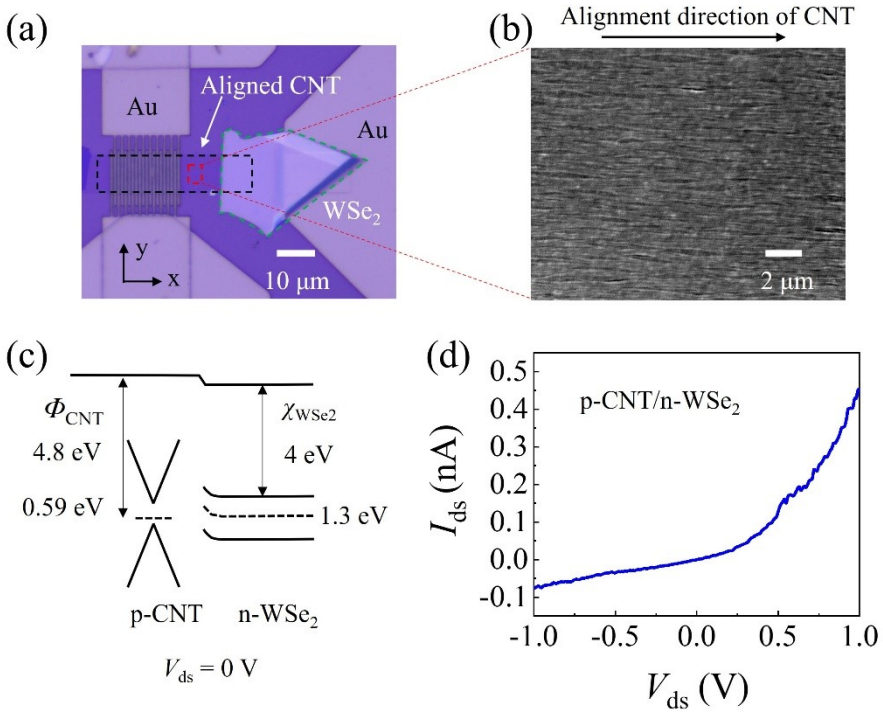


Fig. 2. Band alignment of aligned-CNT/WSe_2 p-n junction. (a) Optical image of aligned-CNT/WSe_2 p-n junction device. The scale bar is 10 μm. (b) The scanning electron microscope (SEM) image of the aligned CNTs shows that the axial direction of the CNTs is parallel to the direction of the applied current. The scale bar is 2 μm. (c) Band alignment of the aligned-CNT/WSe_2 p-n junction at zero bias. The work function of CNTs and the electron affinity of WSe_2 are adopted from References[43,44], respectively. (d) I_{ds}-V_{ds} curve of the aligned-CNT/WSe_2 p-n junction. During the measurements, CNT and WSe_2 were set as the drain and source terminals, respectively. A positive or negative bias voltage was applied to the CNT electrode.

To investigate the light-intensity dependence of the aligned-CNT/WSe_2 heterojunction photodetector, incident optical power densities ranging from 0.08 to

94.8 W/cm² were applied to the device. The laser beam was focused onto the device via a 10× objective lens, with a spot diameter of approximately 115 μm, which is much larger than the device size. Figure 3a presents the $|I_{ds}|$-V_{ds} curves of the CNT/WSe_2 heterojunction under dark conditions and 550 nm laser illumination at various power densities (0.08, 0.68, 4.4, 24, 43.2 and 94.8 W/cm²). A low dark current of -0.076 nA was obtained at -1 V in the dark state. The short-circuit current (I_{short}) and open-circuit voltage (V_{open}) versus incident light intensity are shown in Figs. 3(b) and 3(c). Higher incident power generates more photogenerated carriers, leading to a monotonic increase in short-circuit current, with a maximum value of -89.5 nA. The open-circuit voltage originates from the potential difference resulting from the separation and accumulation of photogenerated carriers driven by the built-in electric field. The heterojunction exhibits a distinct photovoltaic effect, with a maximum open-circuit voltage of 0.26 V.

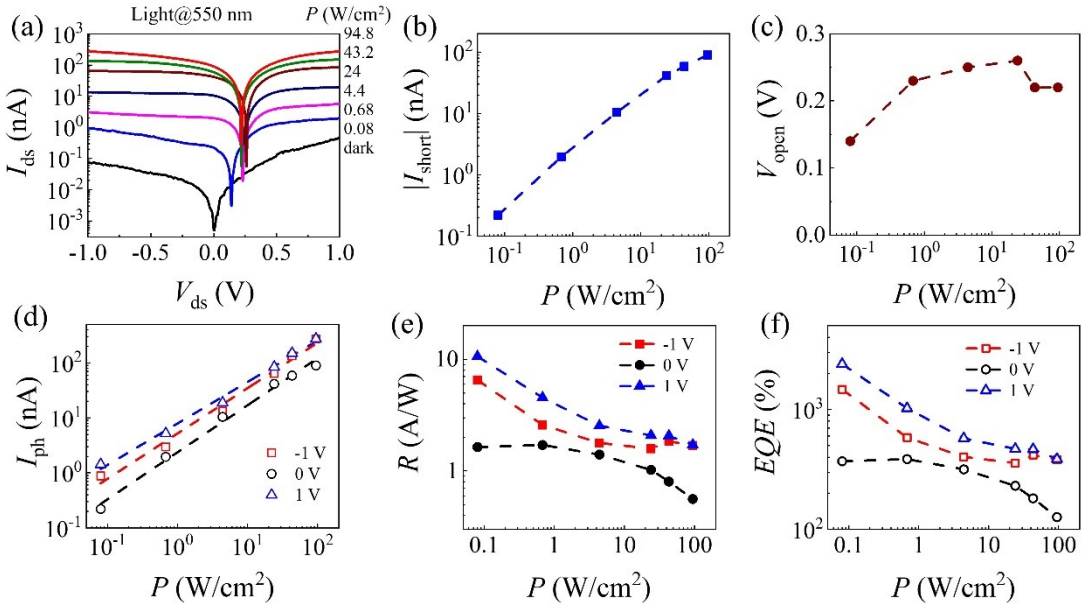


Fig. 3. Light-intensity-dependent optoelectronic properties of aligned-CNT/WSe_2 heterojunction. (a) The $|I_{ds}|$-V_{ds} curves of the device are measured in the dark and under various optical power densities (P = 0.08, 0.68, 4.4, 24, 43.2, 94.8 W/cm²) under 550 nm laser irradiation. The vertical axis represents the absolute value of current on a logarithmic scale. Short-circuit current (b) and open-circuit voltage (c) of the device as a function of incident optical power density. Photocurrent (d), photoresponsivity (e) and EQE (f) versus incident optical power density P under V_{ds} = -1, 0, 1 V.

Under illumination, electron-hole pairs are generated in the aligned-CNT/WSe_2 heterojunction and separated by the electric field, thus producing photocurrent. Photocurrent (I_{ph}) is defined as the absolute difference between the current under illumination and the dark current, namely $I_{ph} = |I_{light} - I_{dark}|$. Figure 3(d) plots the dependence of photocurrent on light-intensity at different biases (V_{ds} = -1, 0, 1V). The photocurrent increases with rising power density and exhibits a sublinear relationship following $I_{ph} \propto P^{\alpha}$.[45] A higher optical power density generates more photogenerated electrons and holes in the heterojunction, which increases the carrier concentration and accordingly the photocurrent. Meanwhile, the carrier recombination probability rises and the carrier lifetime decreases. Fitting results yield the power exponent α of 0.82, 0.75, and 0.8 at V_{ds} = -1, 0, 1 V respectively. All values are less than 1, because increasing light intensity raises the population of photogenerated carriers and enhances Auger recombination, thereby shortening the carrier recombination lifetime. Similar sub-linear responses have been observed in other photodetectors.[46,47] Compared with the bias of 0 V, the α values are higher at -1 V and 1 V. A larger electric field is established under higher bias voltages, which facilitates the separation of photogenerated electron-hole pairs, shortens the carrier transport time in the channel and reduces the carrier recombination probability. The photoresponsivity R of the device is expressed as $R = I_{ph}/PS$, where P is the incident optical power density and S is the effective light-absorption area of the heterojunction (~70 μm^2). Figure 3d presents the variation of R with incident power density under V_{ds} = -1, 0, 1 V. Photoresponsivity increases as the optical power density decreases. A maximum photoresponsivity of ~10.6 A/W is achieved at 1 V. The external quantum efficiency (EQE) of a photodetector is defined as the ratio of the total number of electrons collected by the electrodes to the total number of incident photons, with the formula $EQE = hcR/e\lambda$. Here, h is Planck's constant, c is the speed of light, e is the elementary charge, and λ is the incident light wavelength. Similarly, the EQE declines with increasing optical power density, and the maximum EQE reaches approximately ~2400%. This phenomenon can be attributed to the photoconductive gain effect induced by interfacial traps at the aligned-CNT/WSe_2 heterojunction.[48] Shallow-level traps including Se vacancies and interfacial hybrid energy levels at the CNT-WSe_2 interface selectively trap photogenerated holes and extend the lifetime of photogenerated electrons. As a result, electrons within WSe_2 travel repeatedly across the channel and are collected by the electrodes, which yields photoconductive gain.[49,50] The specific detectivity (D^*) serves as a critical figure-of-merit for photodetectors and is

determined by device noise. Noise in photodetectors stems from multiple sources, such as shot noise, flicker noise, thermal noise, and generation-recombination noise, all of which can be accurately characterized by noise-power-spectrum measurements.[51,52] For simplicity, by assuming shot noise as the dominant noise component, one can use the simplified expression $D^* = RS^{1/2}/(2eI_{dark})^{1/2}$, where e denotes the elementary electron charge.[51,52] Our CNT/WSe_2 photodetector yields a specific detectivity of 7.6 $\times 10^9$ Jones at 1 V under 0.08 W/cm^{-2} illumination. This value would become lower upon consideration of extra noise sources. All these characteristics confirm the desirable optoelectronic properties of the photodetector.

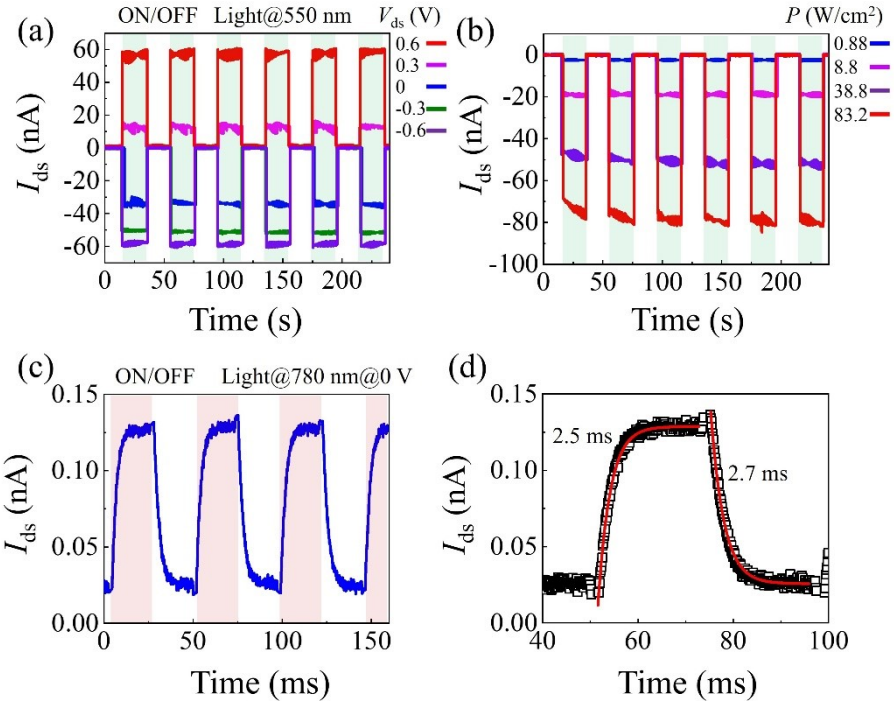


Fig. 4. Operating stability and response time of the aligned-CNT/WSe_2 photodetectors. (a) The operational stability of the device under varying biases (V_{ds} = -0.6, -0.3, 0, 0.3, 0.6 V) was tested under fixed 550 nm illumination with an optical power density of 24 W/cm^2. (b) Operational stability of the device under varying optical power densities (P = 0.88, 8.8, 38.8, 83.2 W/cm^2) in self-powered mode (V_{ds} = 0 V). (c-d) Response time of the device under 780 nm illumination with a fixed power density of 0.05 W/cm² under self-powered mode.

Stable and reproducible photoswitching performance is another crucial characteristic of photodetectors. We investigated the photoswitching response of the

aligned-CNT/WSe_2 heterojunction device under various biases and incident optical power densities. Figure 4(a) presents the operating stability of the photodetector measured at different V_{ds} (-0.6, -0.3, 0, 0.3, 0.6 V) under 550 nm illumination with a fixed power density of 24 W/cm^2. The on/off ratio is defined as the ratio of the current under illumination to the dark current. The ratio exceeds 10^3 at V_{ds} = -0.3 V. Under the self-powered mode (V_{ds} = 0 V), the device exhibits stable and fast photoresponse at various incident power densities (P = 0.88, 8.8, 38.8, 83.2 W/cm^2), as shown in Fig. 4(b). The maximum on/off ratio ~876 was achieved at 550 nm and 38.8 W/cm^2. We further measured the response time of the aligned-CNT/WSe_2 heterojunction photodetector. Figure 4(c) shows periodic variations of photocurrent recorded by an oscilloscope under 780 nm light, a power density of 0.05 W/cm^2 and V_{ds} = 0 V. The dynamic evolution of photocurrent during the rise and decay processes can be described by the following equations[47,53]: $I(t) = I_0[1 - \exp(-(t - t_0)/\tau_R)]$ and $I(t) = I_0[\exp[-(t - t_0)/\tau_D]$, where τ_R and τ_D represent the rise time and decay time, respectively. Fitting analysis on the experimental data yields a rise time of 2.5 ms and a decay time of 2.7 ms, as shown in Fig. 4(d). Therefore, the device possesses favorable photoswitching performance and enables self-powered photodetection.

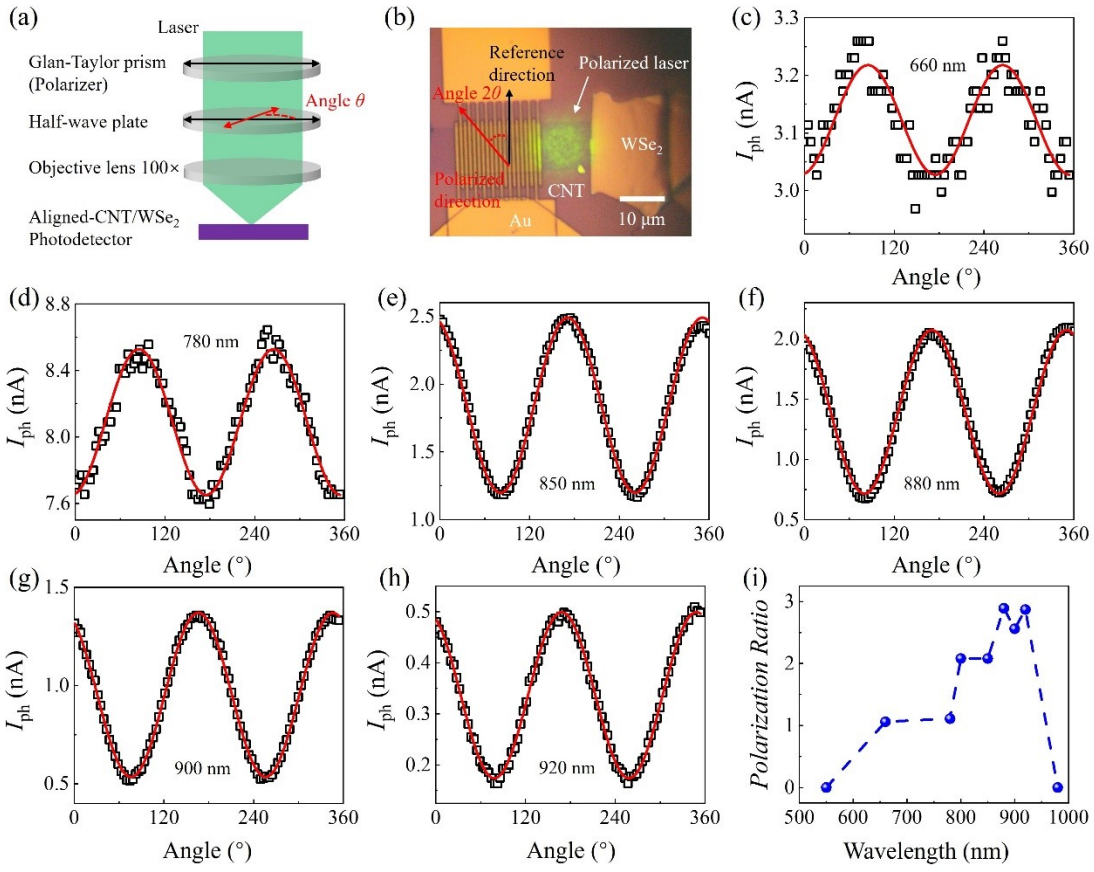


Fig. 5. Polarization-dependent optical absorption of aligned-CNT/WSe_2 photodetectors. (a) Schematic diagram of polarized photocurrent measurement setup. (b) Optical image of the device during measurement. The laser is focused on the aligned-CNT/WSe_2 heterojunction, with a spot diameter of approximately 15 μm. Photocurrent versus incident light polarization angle of the device under laser irradiation at 660 nm (c), 780 nm (d), 850 nm (e), 880 nm (f), 900 nm (g) and 920 nm (h) under self-powered operation mode. The black squares represent experimental data points, and the red curve is the fitting curve. The laser power density was fixed at 45 W/cm^2. (i) Wavelength-dependent polarization anisotropy ratio of the device.

Finally, we investigated the linearly polarized photodetection performance of aligned-CNT/WSe_2 heterojunction devices. The measurement principle is illustrated in Fig. 5(a). Incident parallel light is converted into linearly polarized light via a Glan-Taylor prism, and its polarization direction is adjusted using a half-wave plate. Notably, the actual rotation angle of polarization is twice the rotation angle of the half-wave plate. The light is focused on the aligned-CNT/WSe_2 heterojunction, as shown in the optical micrograph in Fig. 5(b). By rotating the half-wave plate, the polarization angle varies from 0° to 360°, and the corresponding photocurrent responses are recorded synchronously. Figures 5(c-h) present the polarization-dependent photocurrent characteristics of the device at wavelengths of 660 nm, 780 nm, 850 nm, 880 nm, 900 nm, and 920 nm. The photocurrent exhibits a two-fold symmetric behavior, where the maximum and minimum photocurrent values appear along mutually perpendicular directions. These two extreme directions are parallel and perpendicular to the alignment direction of the aligned CNT arrays, respectively. Since WSe_2 shows no polarization-dependent absorption for linearly polarized light, the polarization anisotropy of the photocurrent in the aligned-CNT/WSe_2 heterojunction device originates entirely from the aligned CNT arrays. Notably, the optimal polarization response direction of the device is wavelength-dependent. The maximum photocurrent is obtained along the direction perpendicular to the CNT axis at 660 nm and 780 nm, while it occurs along the direction parallel to the CNT axis in the wavelength range of 850-920 nm. This phenomenon can be mainly attributed to the anisotropic band-structure variation of the heterostructure along different directions. Further detailed analysis is provided in the following section. As the wavelength increases, the transition pathway of photogenerated carriers changes correspondingly. Specifically, carrier transitions switch from the larger-bandgap channel along the CNT axis to the smaller-bandgap channel

corresponding to the direction perpendicular to the CNT axis. The red curves in the figure represent the fitting results, which follow the formula[2]: $I_{ph}(\theta) = I_{pmax}\cos^2(\theta + \varphi) + I_{pmin}\sin^2(\theta + \varphi)$. Here, θ denotes the polarization angle of incident light relative to the reference direction, as shown in Fig. 5(b), I_{pmax} and I_{pmin} are the maximum and minimum photocurrents of the photoresponse, respectively, and φ is the fitting coefficient. The linear polarization anisotropy ratio is defined as I_{pmax}/I_{pmin}. Figure 5(i) presents the polarization anisotropy ratios of the aligned-CNT/WSe_2 heterojunction device at different wavelengths. Specifically, the ratio reaches 2.9 under 880 nm polarized light illumination, which is higher than that of most polarization photodetectors based on aligned CNT films.[25,32-34] We summarize the optoelectronic performance of reported photodetectors based on aligned-CNT films together with our device in Table 1 below. The key parameters include the polarization anisotropy ratio, responsivity, response speed, and operating wavelength range. Among all these devices, our device exhibits the highest polarization anisotropy ratio, which demonstrates the great potential of the CNT/WSe_2 hybrid heterostructure for polarization-sensitive photodetection.

Table 1. Performance of reported photodetectors based on aligned-CNT films.

Photodetector Structure	Responsivity	Specific detectivity [Jones]	Response time [τ_r/τ_d]	Polarization ratio	Wavelength [nm]	Ref.
$SnSe_2$/CNT	0.52 A/W	non	0.7 ms	non	760	[33]
CNT/MoS_2	8.51 A/W	3.74×10^{11}	30 μs/40 μs	non	405-1064	[36]
CNT/MoS_2	88.2 μA/W	4.2×10^{6}	102ms/86ms	1.55	405-785	[34]
TiO_2 nanowire/CNT	7.7×10^{3} A/W	1.35×10^{16}	non	1.5	365	[32]
CNT	28 mV/W	Non	32μs	2	660	[25]
CNT/WSe_2	10.6 A/W	7.6×10^{9}	2.5ms	2.9	880	This work

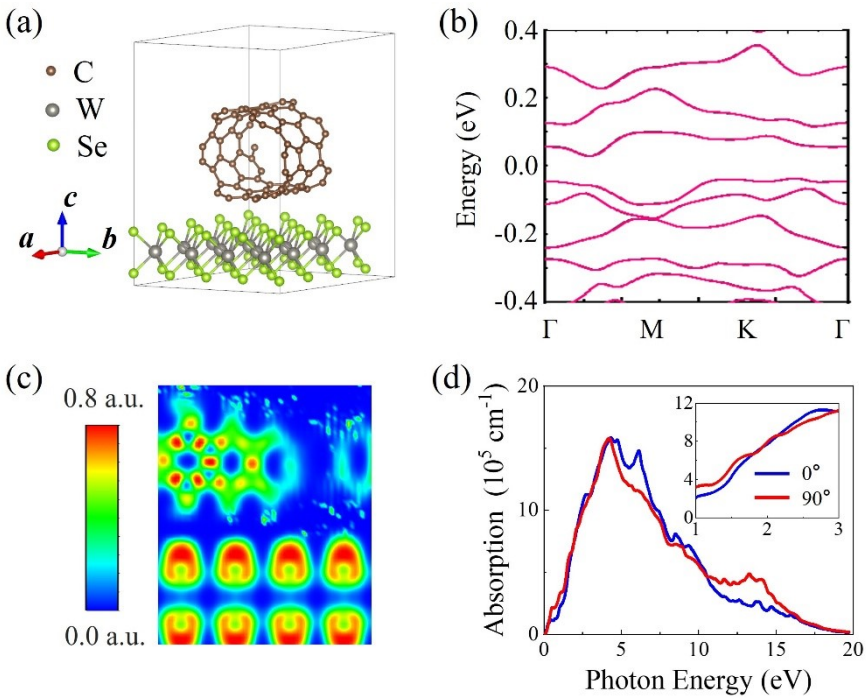


Fig. 6. (a) Schematic diagram of the unit cell for the WSe_2/CNT heterostructure, consisting of monolayer WSe_2 and a single-walled CNT. (b) Band structure of the WSe_2/CNT heterostructure. (c) The electron localization function (ELF) map of the heterostructure. (d) Calculated optical absorption-coefficient curves as a function of photon energy along the 0° and 90° directions. The upper-right inset shows an enlarged view over the photon-energy range of 1-3 eV.

To understand the underlying physical mechanism behind the wavelength-dependent polarized absorption intensities at 0° and 90°, we constructed a WSe_2/CNT heterostructure and calculated the variation of its optical absorption coefficients along the 0°and 90°directions using first-principles calculations. First, the unit cell of the WSe_2/CNT heterostructure is shown in Fig. 6(a). The structural unit adopts P1 symmetry (Space Group No. 1, triclinic system), which allows unconstrained atomic relaxations and avoids imposing artificial symmetry during DFT calculations. The diameter of the CNT is ~1.5 nm, and the interlayer spacing between WSe_2 and the CNT is ~3 Å. The band structure of the heterostructure is presented in Fig. 6(b), which exhibits a distinct energy gap at the Fermi level, indicating that the heterostructure retains its semiconducting character. The electron localization function (ELF) map is displayed in Fig. 6(c). The lower half exhibits a regular ELF distribution for monolayer WSe_2, whereas the upper-region CNT shows an inhomogeneous ELF pattern. This result indicates strong charge transfer inside the

CNT, which leads to pronounced band-structure differences along the axial and perpendicular-to-axis directions of the CNT. Meanwhile, the ELF value is low in the interlayer region between the upper and lower layers, indicating weak van der Waals interactions and the absence of localized interlayer bonding. First-principles calculations based on DFT were performed using VASP. Post-processing of the dielectric-matrix data was carried out with the VASPKIT package to extract the frequency-dependent optical absorption coefficient. The calculated optical absorption coefficients along the 0° and 90° directions are plotted in Fig. 6(d). Multiple intersections appear in the energy-dependent absorption curves (where $wavelength\ (nm) = \frac{1240}{photon\text{-}energy\ (eV)}$), demonstrating that the polarization-resolved absorption intensities vary with wavelength. As shown in the inset of Fig. 6(d), stronger absorption occurs along the CNT axial direction in the photon-energy range of 1.8-3 eV, while larger absorption is obtained along the direction perpendicular to the CNT axis within 1-1.8 eV. This provides a good explanation for our experimental observations. Similar wavelength-dependent evolution of absorption intensity for different polarization directions has also been reported in previous photodetector studies.[54,55] This indicates that the anisotropic band-structure variation of the heterostructure along different directions is the dominant intrinsic physical mechanism responsible for such phenomena.

4. Conclusion

In summary, we have constructed a novel polarization-sensitive photodetector based on a mixed 1D/2D aligned-CNT/WSe_2 heterostructure. The device achieves a high responsivity of 10.6 A/W at 550 nm. Under self-powered mode, it has a response time of 2.5 ms, an on/off ratio of 10^3 and excellent operational stability. Notably, it exhibits prominent polarized absorption in the wavelength range of 660-920 nm. The maximum linear polarization anisotropy ratio reaches 2.9 at 880 nm under self-powered operation. This work lays a solid experimental foundation for the design and fabrication of high-performance polarized photodetectors based on 1D/2D aligned-CNT/semiconductor p-n junctions.

Acknowledgements

This work was supported by the CETC Key Laboratory of Carbon-based Electronics (Grant. No. CKLCE0304202403), the National Natural Science Foundation of China (Grant Nos. 12241405, 12174384 and 12404146).

References

[1] Wang Z, Chen J, Zhu J, Batool H S, Hu J and Wang D 2026 *Langmuir* **42** 10798

[2] Zhu W, Wei X, Yan F, Lv Q, Hu C and Wang K 2019 *J. Semicond.* **40** 092001

[3] Ran W, Ren Z, Wang P, Yan Y, Zhao K, Li L, Li Z, Wang L, Yang J, Wei Z, Lou Z and Shen G 2021 *Nat. Commun.* **12** 6476

[4] Zuo J, Bai J, Choi S, Basiri A, Chen X, Wang C and Yao Y 2023 *Light: Sci. Appl.* **12** 218

[5] Zhang Q, Ni S, Zhang D, Wang Y, Xue Q, Wang Y, Zhang J, Zhu F, Pan C, Shao Y, Liu C and Liang T 2025 *ACS Appl. Mater. Interfaces* **17** 31248

[6] Iijima S 1991 *Nature* **354** 56

[7] Richter M, Heumüller T, Matt G J, Heiss W and Brabec C J 2017 *Adv. Energy Mater.* **7** 1601574

[8] Li Z, Xu K and Wei F 2018 *Nanotechnol. Rev.* **7** 393

[9] Barkelid M, Steele G A and Zwiller V 2012 *Nano Lett.* **12** 5649

[10] Jiang K, Li Q and Fan S 2002 *Nature* **419** 801

[11] Zhang M, Fang S, Zakhidov A A, Lee S B, Aliev A E, Williams C D, Atkinson K R and Baughman R H 2005 *Science* **309** 1215

[12] Kim Y, Minami N, Zhu W, Kazaoui S, Azumi R and Matsumoto M 2003 *Jap. J. Appl. Phys.* **42** 7629

[13] Engel M, Small J P, Steiner M, Freitag M, Green A A, Hersam M C and Avouris P 2008 *ACS Nano* **2** 2445

[14] Cao Q, Han S-j, Tulevski G S, Zhu Y, Lu D D and Haensch W 2013 *Nat. Nanotechnol.* **8** 180

[15] Liu L, Han J, Xu L, Zhou J, Zhao C, Ding S, Shi H, Xiao M, Ding L, Ma Z, Jin C, Zhang Z and Peng L-M 2020 *Science* **368** 850

[16] Eres G, Puretzky A A, Geohegan D B and Cui H 2004 *Appl. Phys. Lett.* **84** 1759

[17] Jiang Q, Wang K, Wang F, Leu K, Li R, Zhao Y, Xi A, Zang Y and Zhang R 2024 *ACS Nano* **18** 25249

[18] Li X, Yu D, Chen J, Wang Y, Cao F, Wei Y, Wu Y, Wang L, Zhu Y, Sun Z, Ji J, Shen Y, Sun H and Zeng H 2017 *ACS Nano* **11** 2015

[19] Arnold M S, Zimmerman J D, Renshaw C K, Xu X, Lunt R R, Austin C M and Forrest S R 2009 *Nano Lett.* **9** 3354

[20] Liu Y, Yin J, Wang P, Hu Q, Wang Y, Xie Y, Zhao Z, Dong Z, Zhu J-L, Chu W, Yang N, Wei J, Ma W and Sun J-L 2018 *ACS Appl. Mater. Interfaces* **10** 36304

[21] Wu W, Ma H, Cai X, Han B, Li Y, Xu K, Lin H, Zhang F, Chen Z, Zhang Z, Peng L-M and Wang S 2023 *ACS Nano* **17** 15155
[22] Cao J, Zou Y, Gong X, Gou P, Qian J, Qian R and An Z 2018 *Appl. Phys. Lett.* **113** 061112
[23] Sarkar K and Kumar P 2024 *Carbon* **219** 118842
[24] Liu Y, Wang F, Wang X, Wang X, Flahaut E, Liu X, Li Y, Wang X, Xu Y, Shi Y and Zhang R 2015 *Nat. Commun.* **6** 8589
[25] Nanot S, Cummings A W, Pint C L, Ikeuchi A, Akiho T, Sueoka K, Hauge R H, Léonard F and Kono J 2013 *Sci. Rep.* **3** 1335
[26] He X, Wang X, Nanot S, Cong K, Jiang Q, Kane A A, Goldsmith J E M, Hauge R H, Léonard F and Kono J 2013 *ACS Nano* **7** 7271
[27] Dai W, Liu W, Yang J, Xu C, Alabastri A, Liu C, Nordlander P, Guan Z and Xu H 2020 *Light: Sci. Appl.* **9** 120
[28] Lee J U 2005 *Appl. Phys. Lett.* **87** 073101
[29] Abdula D and Shim M 2008 *ACS Nano* **2** 2154
[30] Liu C-H, Wu C-C and Zhong Z 2011 *Nano Lett.* **11** 1782
[31] Zeng Q, Wang S, Yang L, Wang Z, Pei T, Zhang Z, Peng L-M, Zhou W, Liu J, Zhou W and Xie S 2012 *Opt. Mater. Express* **2** 839
[32] Li M, Wang Z, Jin Y, Yang H, Zhang L, Li H, Wang J, Fan S and Li Q 2023 *Nano Lett.* **23** 6059
[33] Tannarana M, Pataniya P and Solanki G K 2024 *J. Mater. Sci. Mater. Electron.* **35** 1671
[34] Huang P-Y, Chen H-J, Qin J-K, Zhen L and Xu C-Y 2022 *Nanoscale Adv.* **4** 5290-5296
[35] Ahmad W, Tareen A K, Khan K, Khan M, Khan Q, Wang Z and Maqbool M 2023 *Appl. Mater. Today* **30** 101717
[36] Wang K, Wang F, Cao Y, Jiang Q, Xi A, Leu K, Wang X, Zang Y, Liu R and Zhang R 2025 *Adv. Funct. Mater.* **35** 2421980
[37] Zhou C, Zhao Y, Raju S, Wang Y, Lin Z, Chan M and Chai Y 2016 *Adv. Funct. Mater.* **26** 4223-4230
[38] Zhu W, Wen H, Zhu S, Cui Q, Xie S, Ye M, Zhang G, Wu H, Zhang X, Li W, Huang Y, Zhang J, Zhao L, Patanè A, Chang H, Wang L-W and Wang K 2025 *Nat. Commun.* **16** 9509
[39] Pudasaini P R, Oyedele A, Zhang C, Stanford M G, Cross N, Wong A T, Hoffman A N, Xiao K, Duscher G, Mandrus D G, Ward T Z and Rack P D 2018 *Nano*

Research **11** 722
[40] Huang H-Y, Chou C-H, Chiu H-Y, Hsu Y-W, Wu Q-Y, Liu B-H, Kei C-C and Chien C-H 2026 *ACS Appl. Electron. Mater.* **8** 256
[41] Saito R, Fujita M, Dresselhaus G and Dresselhaus M S 1992 *Appl. Phys. Lett.* **60** 2204
[42] Yan F, Wei Z, Wei X, Lv Q, Zhu W and Wang K 2018 *Small Methods* **2** 1700349
[43] Suzuki S, Bower C, Watanabe Y and Zhou O 2000 *Appl. Phys. Lett.* **76** 4007
[44] Wei X, Yan F, Lv Q, Shen C and Wang K 2017 *Nanoscale* **9** 8388
[45] Hu P, Wen Z, Wang L, Tan P and Xiao K 2012 *ACS Nano* **6** 5988
[46] Massicotte M, Schmidt P, Vialla F, Schädler K G, Reserbat-Plantey A, Watanabe K, Taniguchi T, Tielrooij K J and Koppens F H L 2016 *Nat. Nanotechnol.* **11** 42
[47] Yan F, Zhao L, Patanè A, Hu P, Wei X, Luo W, Zhang D, Lv Q, Feng Q, Shen C, Chang K, Eaves L and Wang K 2017 *Nanotechnology* **28** 27LT01
[48] Jin Y, Keum D H, An S-J, Kim J, Lee H S and Lee Y H 2015 *Adv. Mater.* **27** 5534
[49] Shin G H, Park C, Lee K J, Jin H J and Choi S-Y 2020 *Nano Lett.* **20** 5741
[50] Chen Y, Liang X, Liu S, Huang Z, Wu Z, Liu X, Xiao Z, Peng X, Shi X and Zhao H 2024 *Adv. Mater. Technol.* **9** 2302095
[51] Wang F, Zhang T, Xie R, Wang Z and Hu W 2023 *Nat. Commun.* **14** 2224
[52] Wang Y, Chen J, Hu T, Huang Y, Zhu W, Li W, Hu Y, Wei Z, Fan Z, Zhao L and Wang K 2025 *Small* **21** 2407473
[53] Lv Q, Yan F, Wei X and Wang K 2018 *Adv. Opt. Mater.* **6** 1700490
[54] Bai L, Yang Z, Wen J, Mai Z, Liu B, Liu D, Ci P, Liu L, Xie Y, Zhou Z, Yu Y and Wei Z 2025 *Chip* **4** 100143
[55] Zhou Z, Shen T, Wang P, Guo Q, Wang Q, Ma C, Xin K, Zhao K, Yu Y, Qin B, Liu Y-Y, Yang J, Hong H, Liu K, Liu C, Deng H-X and Wei Z 2023 *Sci. Bull.* **68** 173